

Robust Airfoil Optimization and the Importance of Appropriately Representing Uncertainty

Laurence W. Cook* and Jerome P. Jarrett†

Department of Engineering, University of Cambridge, Trumpington Street, Cambridge, CB21PZ.

ABSTRACT

The importance of designing airfoils to be robust with respect to uncertainties in operating conditions is well recognized. However, often the probability distribution of such uncertainties does not exist or is unknown, and a designer looking to perform a robust optimization is tasked with deciding how to represent these uncertainties within the optimization framework. This paper asks “how important is the choice of how to represent input uncertainties mathematically in robust airfoil optimization?”, specifically comparing probabilistically based aleatory uncertainties and interval based epistemic uncertainties. This is first investigated by considering optimizations on several algebraic test problems, which illustrate the mechanisms by which the representation of uncertainty becomes significant in a robust optimization. This insight is then used to predict and subsequently demonstrate that for two airfoil design problems the advantage of doing a robust optimization over a deterministic optimization is similar regardless of how the input uncertainties are represented mathematically. The benefit of this is potentially eliminating the time required to establish an accurate representation of the uncertainties from the preliminary stage of design, where time is a valuable resource.

This is the authors’ copy of the accepted manuscript. The published version is located at the following DOI: 10.2514/1.J055459, and was published online in AIAA Journal on July 27th 2017. Copyright 2017 Laurence W. Cook & Jerome P. Jarrett.

Nomenclature

\mathbf{x}	Design variables
n_x	Number of design variables
\mathbf{x}^*	Design variables for optimal solutions
Y	System model output / quantity of interest
\mathbf{u}	Uncertainty vector
x_i^l	Lower bound of i^{th} design variable
x_i^u	Upper bound of i^{th} design variable
g_j	j^{th} constraint function
n_g	Number of constraints
ϕ_k	Polynomial basis function
a_k	Expansion coefficient
M	Truncation of expansion

*PhD Candidate, Department of Engineering, University of Cambridge. Student Member AIAA. Email: lwc24@cam.ac.uk

†University Lecturer, Department of Engineering, University of Cambridge. Senior Member AIAA. Email: jpp1001@cam.ac.uk

p	Polynomial chaos order in each dimension
μ	Mean
σ	Standard deviation
f_p	Measure of performance
f_r	Measure of robustness
w_p	Performance measure weighting
w_r	Robustness measure weighting
Δ	Magnitude of uncertainty
v	Parameter subject to uncertainty
u	Underlying uncertain variable
C_L	Lift coefficient
C_D	Drag coefficient
L/D	Lift to drag ratio

1 Introduction

Airfoils are at the heart of many aerospace applications (e.g. aircraft wings, turbomachinery, rotors), and like many engineering systems their design can now benefit significantly from the use of computational optimization [1]. However, deterministically optimized systems often lie in extreme regions of the design space, and when realized, their performance is often worse than predicted due to uncertainties in the design process. In airfoil design this phenomenon manifests itself as “kinks” in performance polars when only a single operating condition is considered in the optimization [2, 3]. Therefore the importance of taking account of uncertainties is becoming increasingly recognized both for airfoil design and engineering design in general [4]. Robust optimization (RO) is the general optimization framework that obtains designs which maintain good performance under uncertainties [5].

Uncertainties are usually classified as either aleatory (irreducible) or epistemic (due to a lack of knowledge) [6–8], and different mathematical representations and propagation methods are appropriate for each type. In order to accurately resolve the probability distribution of an uncertainty like Mach number, for example, historical data on operating conditions could be used to obtain a histogram. However this data may not exist (if it is for a new concept), could be sparse, or could be hard to obtain. Therefore, most uncertainties are somewhat epistemic early in the design process, but a designer wishing to perform a robust optimization must decide how to represent each of the uncertainties mathematically and use a pertinent uncertainty propagation technique.

This raises the question of how much this decision affects the results of a robust optimization. From the perspective of accurately quantifying the uncertainty on the QOI, it is important to represent these input uncertainties appropriately, as one might expect. Studies into uncertainty quantification in aerospace applications [9, 10] illustrate that erroneous output uncertainty levels are predicted if all input uncertainties are assumed to be aleatory, leading to the development of methods for mixed interval and probabilistic uncertainty quantification techniques [11, 12]. However, different quantifications of output uncertainty do not necessarily mean different outcomes of a robust optimization, and so in this paper we present an investigation into the effect of uncertainty representation on the results of robust airfoil shape optimizations.

In section 2 we provide background into robust airfoil design, robust optimization in general and different types of uncertainties. In section 3 we perform investigations on algebraic test problems to identify the mechanisms by which the mathematical representation of uncertainties affects robust optimizations. In section 4 we apply this insight to an exploratory airfoil design problem: the robust lift to drag ratio maximization of an airfoil subject to multiple input uncertainties in inviscid flow conditions; this is a problem that is known to give a significant trade-off between mean performance and robustness. Then in section 5, we apply the insight to practical airfoil design problem: a robust drag minimization subject to lift and geometric constraints and uncertain Mach number in viscous transonic flow. Finally in section 6 we conclude the paper.

2 Background

The limitation of deterministic airfoil optimization was noted in [2], where it was observed that an optimizer will exploit the smallest possible length scales allowed by the airfoil’s parametrization scheme to improve the performance only at the operating points considered, giving rise to “kinks” in the airfoil polars at these points. It was recommended that multiple operating points should be sampled, where this number is of the same order as the number of design parameters, so that performance is increased over a larger range of operating conditions: the multi-point approach to airfoil design. This approach was later extended to be equivalent to a more formal probability based approach where the weights and points are chosen to represent an integration of a PDF so that the expected value is explicitly optimized [3, 13]. Minimizing the expected value of performance by considering multiple operating conditions has since been successfully applied to robust airfoil optimization [14–17].

However, it is also recognized in the field of RO that only considering expected value in an optimization does not take into account variation around this expected value, and so the classical approach to RO also considers a measure of robustness (e.g. variance), and optimizes the trade-off between these two objectives; [5] provides a good overview of RO. Applications of this more formal approach to optimization in airfoil design are more recent and limited [18].

Considering the robustness of the quantity of interest usually makes the problem multi-objective, since expected performance and robustness frequently represent conflicting objectives in an optimization [19, 20]. Therefore the general formulation of a robust optimization problem can be expressed as:

$$\begin{aligned} \underset{\mathbf{x}}{\text{minimize}} \quad & [f_p(Y(\mathbf{x}, \mathbf{u})), f_r(Y(\mathbf{x}, \mathbf{u}))] \\ \text{subject to} \quad & x_i^l \leq x_i \leq x_i^u \quad i = 1, \dots, n_x \\ & g_j(\mathbf{x}) \leq 0 \quad j = 1, \dots, n_g \end{aligned} \tag{1}$$

where Y is the output quantity of interest to be minimized (e.g. drag), g_j are the constraints on the design, and f_p and f_r represent measures of performance and robustness of Y respectively; under a probabilistic framework, for example, these are commonly the mean and standard deviation (or variance).

The practical solution of this optimization problem, given a mathematical representation of the input uncertainties, requires this information on the uncertain inputs to be propagated through to the quantity of interest, Y , to obtain the objectives f_p and f_r . We refer to the two steps of representing and propagating uncertainties together as uncertainty quantification (UQ). In RO the UQ inner loop is embedded in an optimization outer loop which modifies the design variables \mathbf{x} in order to minimize f_p and f_r , as illustrated in Figure 1.

Considering Figure 1, representing the uncertainty differently (and using the corresponding propagation technique) can be thought of as exchanging the uncertainty propagation box for different methods of evaluating the deterministic model of Y at different values of \mathbf{u} in order to provide measures of performance and robustness to the optimization outer loop.

2.1 Representations of Uncertainty

A number of different approaches to representing both aleatory and epistemic uncertainties mathematically are available. Aleatory uncertainties are irreducible uncertainties due to unavoidable random behavior [6, 21]: theoretically the probability density function (PDF) could be obtained if enough data is available since they are due to a natural random process, so they are usually treated within a probabilistic framework. However, as mentioned in Section 1, actually obtaining an accurate PDF for input uncertainties is often a challenge in itself.

Epistemic uncertainties are fundamentally due to a lack of knowledge and various methods of quantifying them are possible [22]; these methods lie on a spectrum from probabilistic where the structure is assumed to be known to intervals where the structure is completely unknown (with techniques such as evidence theory in between [7, 12]).

Since it would be infeasible to investigate all possible representations of uncertainty, this paper uses four that are thought to be representative of the literature and enough to perform a useful investigation: assign a uniform distribution, assign a

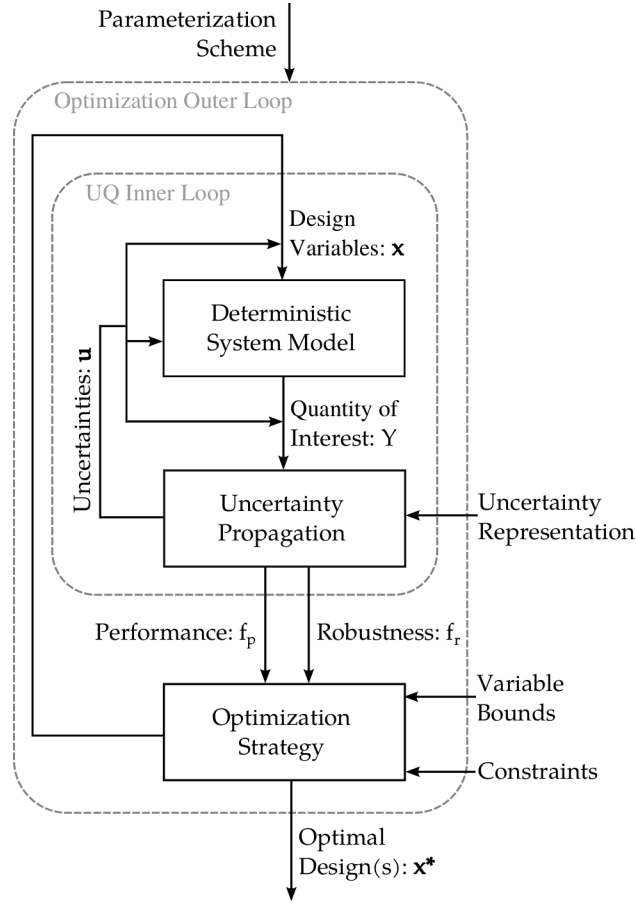


Figure 1: Illustration of how uncertainty quantification fits as an inner loop within a robust optimization.

beta distribution, assign a Gaussian/Normal distribution, and assign an interval. The question under investigation concerns primarily the choice between probabilistic and interval representations of uncertainty (representing the choice of aleatory or epistemic), but we also consider common PDFs assigned to aleatory uncertainties, since even if a probabilistic framework is the appropriate representation, it is useful to investigate how much the choice of PDF may affect the outcome of the optimization. This is implemented by treating uncertain variables in the form:

$$v = v_{nom} + \Delta \times u \quad (2)$$

where v_{nom} is the nominal value of an uncertain parameter (which could be a design variable or system parameter), u represents the fundamental uncertainty, and Δ is a scaling variable to represent the magnitude of the uncertainty. The magnitude of Δ will depend on the specific uncertainties in a problem and is separate to the mathematical representation of u . When u is uniform or Gaussian, its standard deviation is kept consistent, so it is either uniformly distributed between -1 and 1 or normally distributed with zero mean and standard deviation $1/\sqrt{3}$. When a beta distribution is used, the parameters are set to $\alpha = 2$, $\beta = 2$ and the range is over [-1,1], and when interval analysis is used these same bounds, [-1,1], are used. These forms of u are illustrated in figure 2.

2.2 Uncertainty Propagation

Once the mathematical representation of the input uncertainties in \mathbf{u} has been established, they need to be propagated through the system model to obtain the measures of performance and robustness of the QOI (f_p and f_r) which are fed to the optimizer. A lot of previous work in the fields of UQ and OUU has been done developing accurate and computationally

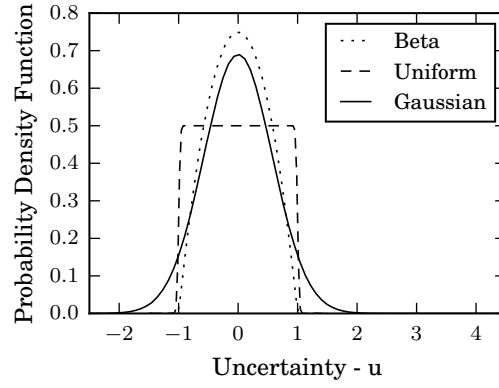


Figure 2: The uncertainty types investigated: uniform and Normal distributions of standard deviation $\frac{1}{\sqrt{3}}$, beta distribution over $[-1,1]$ with parameters $\alpha = 2$, $\beta = 2$, and an interval over $[-1,1]$.

efficient methods to achieve this, and common methods include sampling based approaches, quadrature based approaches, Taylor series based approaches (also sometimes known as moment methods), and stochastic expansion based methods [23].

From the point of view of this investigation, since we are interested in the representation of uncertainties, the propagation is just an intermediate step. Therefore we simply require techniques of sufficient accuracy to effectively propagate the relevant input uncertainties; in the following we highlight the methods used and where they fit within the literature.

2.2.1 Polynomial Chaos

Polynomial chaos (which has been used successfully many times in robust optimization [9, 24–26]) is an attractive propagation technique partly because it creates a response surface approximation to the actual system output, which can be used to propagate different types of uncertainties [9, 11]. It obtains a spectral expansion of the output of a random process (which in the robust optimization case is the QOI, Y , at a given \mathbf{x} : \mathbf{x}_{design}) with respect to the uncertain input variable vector $\mathbf{u} = u_1, \dots, u_n$, which is truncated to M terms for practical implementation:

$$Y(\mathbf{u}, \mathbf{x}_{design}) = \sum_{k=0}^{\infty} a_k \phi_k(\mathbf{u}) \simeq \sum_{k=0}^M a_k \phi_k(\mathbf{u}) \quad (3)$$

where $\phi_k(\mathbf{u})$ are the polynomial basis functions (which are orthogonal with respect to a weighting function defining the basis) and a_k are the coefficients of the expansion. The coefficients, a_k , can be found non-intrusively using a Gaussian quadrature based integration of projections of the system onto each basis function in turn, requiring $(p+1)^n$ system evaluations where p is the polynomial order and n is the number of uncertainties (the dimensionality of the uncertainty space). We refer the reader to the literature for further details on non-intrusive polynomial chaos (NIPC) [27, 28].

2.2.2 Probabilistic Analysis for Aleatory Uncertainties

In a polynomial chaos expansion, if the weighting function of the polynomial basis matches the input uncertainty distribution (e.g. via the Askey scheme [29]), then statistical moments of the output can be obtained analytically from the coefficients of the expansion:

$$\mu = a_0, \quad \sigma^2 = \sum_{k=1}^M a_k^2 \quad (4)$$

This is the method used in this paper for obtaining the mean and standard deviation of a QOI under probabilistic input uncertainties (f_p and f_r).

We also note that since this NIPC method uses fixed quadrature points for a given representation of the uncertainty throughout an optimization, finding this NIPC expansion to obtain the mean performance is similar to multi-point optimization for robust airfoil design, except the weights and points are chosen to give the expectation under a given input PDF with optimally chosen integration points. However, using the expansion we are explicitly considering the standard deviation of performance in a formal robust optimization, which is not traditionally done in a multi-point approach.

2.2.3 Interval Analysis for Epistemic Uncertainties

When uncertainties are represented as intervals, they are propagated to produce a single output interval for the QOI. This can be achieved for non-linear problems using optimization [30], where over the input uncertainty domain defined by the intervals, the minimum and maximum outputs are found (also a non-intrusive approach). From this, the midpoint and range of the output interval are used as f_p and f_r [31]. Figure 3 compares this to probabilistic UQ, where an entire PDF is propagated and mean and variance used.

When evaluating the system model is expensive, like in airfoil design when CFD is being used, propagating the intervals will also become expensive. To alleviate this, a response surface over the local uncertainty space can be used instead of the original simulation. A polynomial chaos stochastic expansion creates such a response surface, and this is how interval uncertainties are propagated in this paper: a gradient based optimizer is run twice to find the maximum and minimum value of the polynomial chaos expansion over the uncertain variables' range.

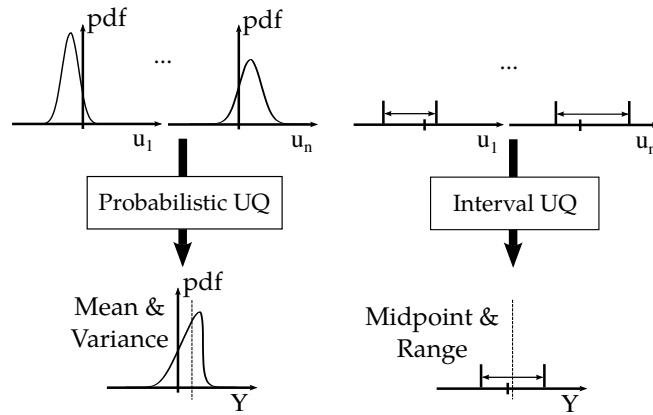


Figure 3: Illustration of probabilistic and interval uncertainty propagation, where n input uncertainties (\mathbf{u}) are propagated through to the quantity of interest Y resulting in measures of performance and robustness.

3 Algebraic Investigations

Before considering airfoil design directly, in this section we first perform investigations on algebraic test problems (so that many optimizations can be performed) in order to identify mechanisms by which the type of uncertainty representation affects a robust optimization trading off f_p and f_r . For this, three test functions are considered, each with varying degrees of complexity and multimodality; they are plotted in figure 4 and detailed below. TP2 and TP3 are adapted from benchmark problems for robust optimization research suggested in [32].

All three use two design variables to facilitate visualization of design space, and uncertainty is only introduced on the design variables themselves to facilitate understanding their behavior and to make it straightforward to identify areas of design space that are robust with respect to these uncertainties (flat regions). They are functions of z_i , $i \in \{1, 2\}$, which are determined from a nominal value (the design variable) x_i , and its associated uncertainty u_i :

$$z_i = x_i + \Delta_i u_i \quad (5)$$

where Δ_i is the magnitude of the uncertainty associated with variable i (see section 2.1). We note that only considering uncertainties on the design variables for these problems does not lose generality, since they are still quantities of the form $Y(\mathbf{x}, \mathbf{u})$. In the general case it is the non-linear behavior of $Y_{\mathbf{x}}(\mathbf{u}) := Y(\mathbf{x}, \mathbf{u})$ at a given design \mathbf{x} that is of interest; we only consider uncertainty around the design variables for these test problems to facilitate visualization and understanding of this non-linear behavior.

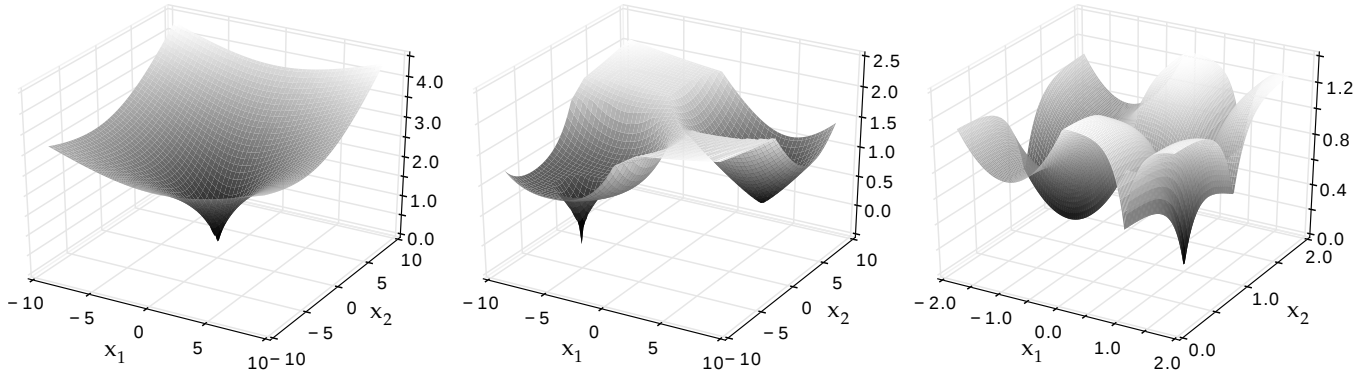


Figure 4: The three test functions: TP1, TP2, and TP3 (from left to right).

TP1:

$$f(\mathbf{z}) = \sqrt{\|\mathbf{z}\|} + (z_2/20)^2 + z_2/15$$

$$x_i \in [-10, 10]$$

TP2:

$$\begin{aligned}
f(\mathbf{z}) &= \frac{5}{5 - \sqrt{5}} - \max(f_0(\mathbf{z}), f_1(\mathbf{z}), f_2(\mathbf{z}), f_3(\mathbf{z})) \\
f_0(\mathbf{z}) &= \frac{1}{10} \exp(0.5 \|\mathbf{z}\|) \\
f_1(\mathbf{z}) &= \frac{5}{5 - \sqrt{5}} \left(1 - \sqrt{\frac{\|\mathbf{z} + 5\|}{5\sqrt{N}}} \right) \\
f_2(\mathbf{z}) &= \frac{625}{624} \left(1 - \sqrt{\frac{\|\mathbf{z} + 5\|}{5\sqrt{N}}} \right)^4 \\
f_3(\mathbf{z}) &= 1.5975 \left(1 - \sqrt{\frac{\|\mathbf{z} + 5\|}{5\sqrt{N}}} \right)^{1.1513} \\
x_i &\in [-10, 10]
\end{aligned}$$

TP3:

$$\begin{aligned}
f(\mathbf{z}) &= 1.3 - \frac{1}{2} (f_1(z_1) + f_2(z_2)) - 0.1z_1 - 0.05z_2 \\
f_i &= \begin{cases} -(z_i + 1)^2 + 1 & \text{for } -2 \leq z_i < 0 \\ 1.32^{-8|z_i - 1|} & \text{for } 0 \leq z_i < 2 \end{cases} \\
x_1 &\in [-2, 2] \\
x_2 &\in [0, 2]
\end{aligned}$$

The fraction of the overall design variable's range that the uncertainty covers is referred to as Δ_{rel} ($\Delta_{rel} = \Delta_i / \text{range}(x_i)$), and in this section the same Δ_{rel} is used for both design variables.

3.1 Preliminary Discussion

Before performing optimization based investigations on these test functions, it is useful to consider the fundamental differences between propagating probabilistic and interval uncertainties to obtain f_p and f_r .

The first key difference can be understood by considering a non-linear system which maps several uniformly distributed inputs to an output; even though all the inputs follow uniform distributions, since the system is non-linear, the output PDF may look radically different, it could be skewed, have one or more peaks of different heights, etc. However under an interval analysis none of this structure is assumed or propagated: all that is known is the output interval. Figure 5 sketches different PDFs over the same interval, illustrating how the skewness leads to the mean differing to the midpoint. It also illustrates how PDFs with different shapes give rise to different variances, demonstrating how using different input PDFs for probabilistic uncertainties can give rise to differing f_p or f_r measures and that the variance is not necessarily proportional to the interval range.

The second difference is revealed by considering how the measures of f_r vary over design space for a particular problem. Figures 6 and 7 plot contours of the relevant measures of f_r for TP1 under (uniform) probabilistic uncertainties and interval uncertainties respectively for very small Δ_{rel} values (so the first effect discussed has negligible influence).

Here we observe that although the overall direction of the contours is similar on both figures, the interval range landscape is distorted so that along certain lines in design space, the interval range is reduced relative to the corresponding variance. This is due to the alignment of the direction of ∇Y (as a function of \mathbf{u} at fixed \mathbf{x}) with one of the uncertainties, as illustrated in figure 7. Since a local uncertainty space defined using intervals is always a hyper-rectangle, when the change in Y over this space aligns with one of its diagonals, it enlarges the range of possible Y values compared to when it is aligned with one of the axes, even if the shape of the response of Y is the same.

This is an effect which is only seen when there is more than one uncertainty, since for a one dimensional problem the interval is always aligned with the gradient of Y . Furthermore, it is enhanced for this test problem because the uncertainties

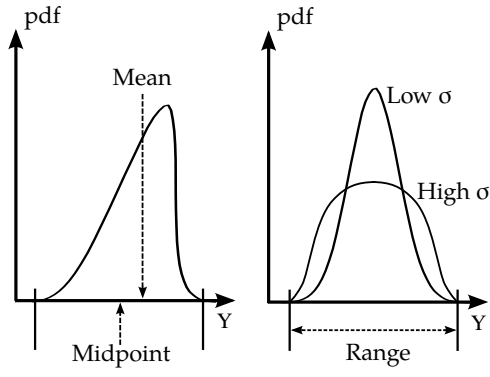


Figure 5: Differences in f_p and f_r between propagating different types of uncertainties.

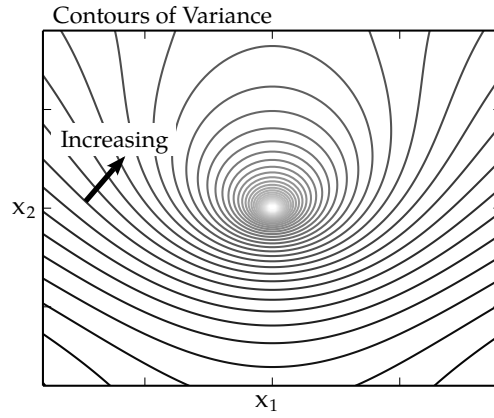


Figure 6: $\log_{10}(\sigma^2)$ contours for TP1 under uniform uncertainties with $\Delta_{rel} = 0.1\%$

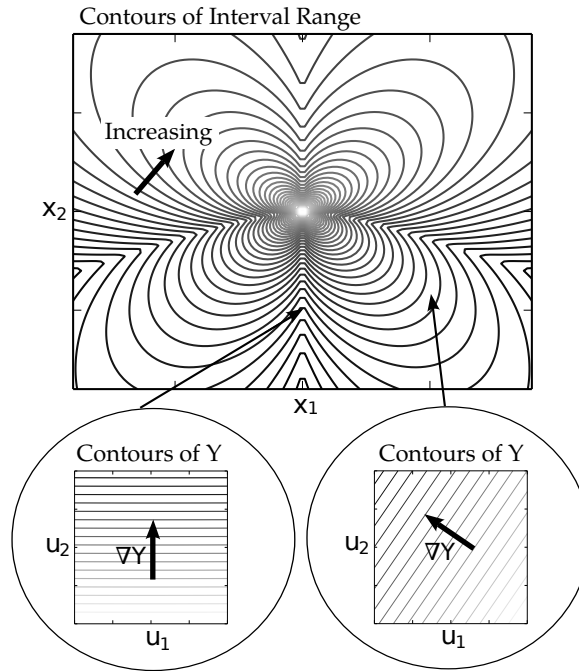


Figure 7: $\log_{10}(\text{range})$ contours for TP1 under interval uncertainties with $\Delta_{rel} = 0.1\%$, and the local landscape of Y as a function of \mathbf{u} at the points $\mathbf{z} = [0, -5]$ and $\mathbf{z} = [5, -5]$

are exclusive to design variables, and so alignment of ∇Y with the uncertainty space changes significantly. However, when uncertainty is also on system parameters (e.g. Mach number), one would expect this alignment to change less significantly over design space.

3.2 Optimization Setup

Now we investigate what impact these differences have on the results of a robust optimization. The NSGA-II algorithm [33] is a common and efficient global multi-objective optimization algorithm used in practice for bi-objective robust optimization [20], and so is the optimizer used for all optimizations in this paper. It is an evolutionary based algorithm, where at each iteration a population of candidates are selected, combined and mutated to produce offspring which can replace candidates for the next generation based on non-dominance. The use of algebraic test functions allows the repetition of optimizations many times to reduce the influence of the stochastic algorithmic decisions on the observations.

The uncertainties are propagated using the NIPC method described in section 2.2; an order 3 NIPC expansion is used (using a total of 16 function evaluations per design point for the 2D uncertainties in the test cases).

For these investigations, Δ_{rel} is varied to be different values, from 0.1% up to 100%, and the goal is to identify how similar robust optimizations using different UQ methods are under different magnitudes of uncertainty for the three test problems. For these problems, for clarity, we consider three uncertainty representations: uniform distribution, Gaussian distribution and interval.

3.3 Optimization Heat-maps

Since we are essentially interested in the impact of the UQ method on how a multi-objective optimization method selects designs, in order to compare optimizations under different uncertainty types we look at design space through the creation of so called “heat-maps”.

These heat-maps are obtained as follows: 50 NSGA-II optimizations (each using a population size of 50 over 20 generations) for each UQ method are performed, every time a candidate design is selected to remain in the population of the algorithm it is recorded, and then a PDF over design space is plotted using kernel density estimation with all of these recorded points as sample data. Figure 8 gives an example of a heat-map created from 50 optimizations of TP2 where the input uncertainties are quantified using uniform distributions.

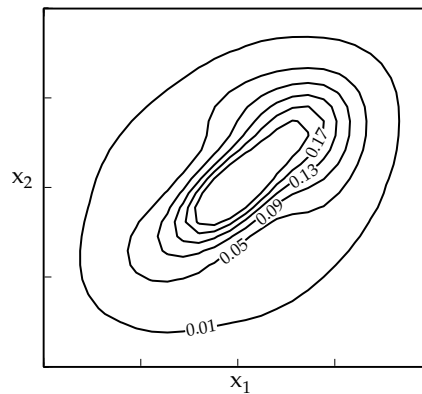


Figure 8: Demo heatmap for part of the design space of TP2 under uniformly distributed probabilistic uncertainties, with contours of heatmap probability values labeled.

The idea is to quantify which areas of design space a robust optimization converges to and finds non-dominated designs in, and it is thought that creating heat-maps like this is more revealing than only looking at the Pareto fronts which result from the optimizations. The selection operator in the NSGA-II algorithm includes designs in lower ranks of non-domination

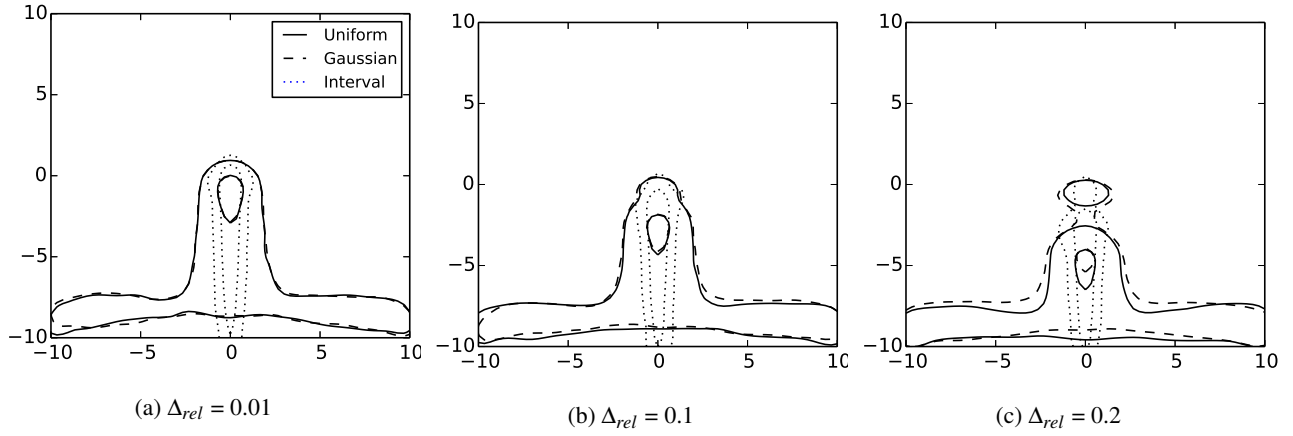


Figure 9: Heat-maps for TP1 at relative uncertainty magnitudes of 0.01, 0.1 and 0.2

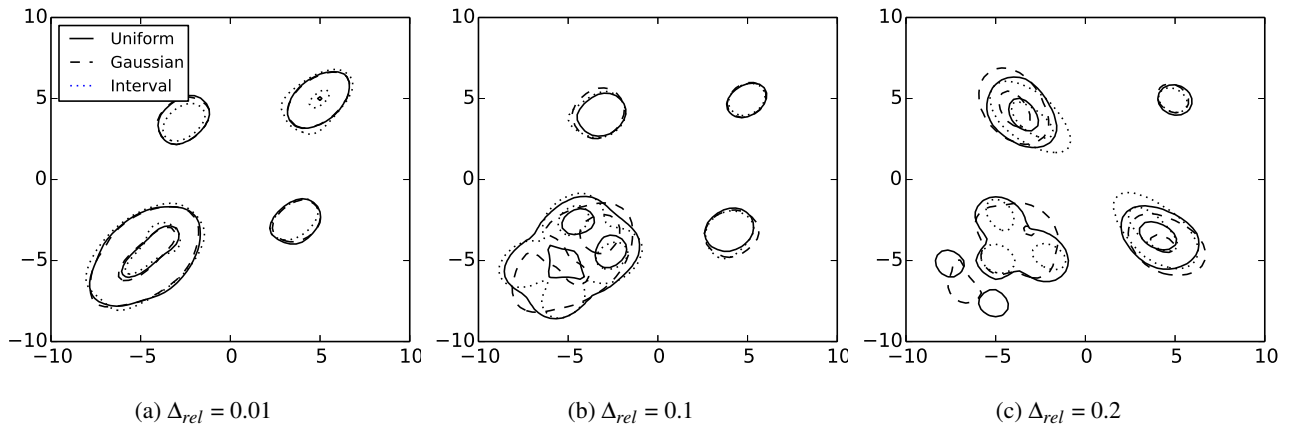


Figure 10: Heat-maps for TP2 at relative uncertainty magnitudes of 0.01, 0.1 and 0.2

(designs that would be non-dominated if the designs on the Pareto front were removed), which highlights any multi-modality introduced into the function as a result of considering robustness, which could be lost if only the Pareto front is considered.

3.4 Results

Analysis of the results found by obtaining heat-maps for different values of Δ_{rel} for the three test problems is given here. What we are actually interested in can be thought of as a “signal to noise ratio”, where the signal is the designs the optimizer would select under the “true” uncertainty representation, and the noise is the error introduced by using a different representation. This section examines the heat-map contours themselves to visualize this ratio, and then quantifies the difference between the heat-maps as a measure of this ratio.

3.4.1 Heat-map Contours

Figures 9, 10 and 11 give the heat-maps for TP1, TP2 and TP3 respectively (showing only the contours at heat-map probability values of 0.02 and 0.15 for clarity) at three values for Δ_{rel} .

On Figure 9a (for TP1 and $\Delta_{rel} = 0.01$) the uniform and Gaussian heat maps are very similar, whereas the interval heat-map is noticeably different. The peak is in the same location, but the robust area of design space is much more focused around $x_1 = 0$ due to the effect illustrated by Figure 7. For the other two test problems, this effect becomes less pronounced, and for low uncertainty magnitudes the heat-maps for all three UQ methods are very similar. This indicates how the effect from Figure 7 essentially distorts peaks on the interval heat-maps compared to the probabilistic ones, but if overall design

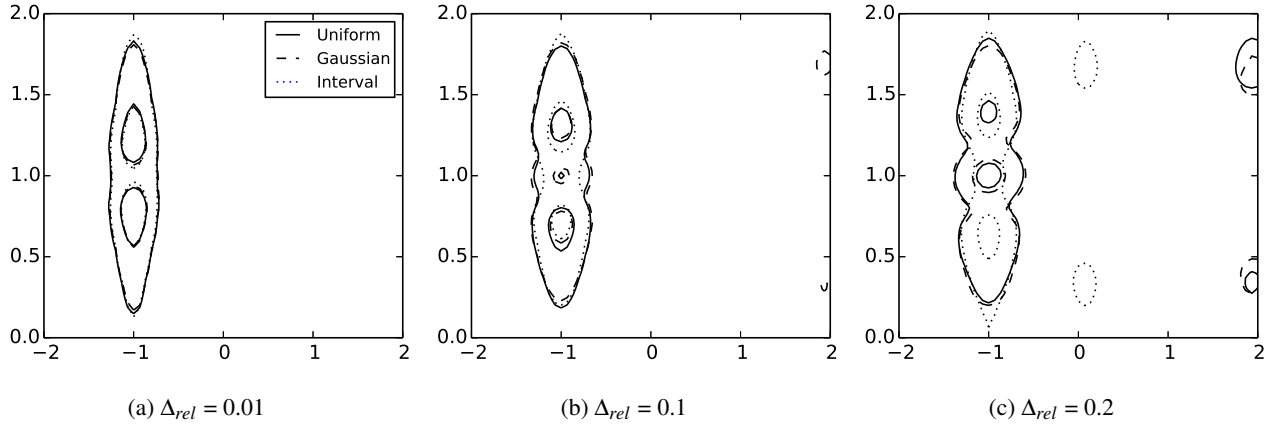


Figure 11: Heat-maps for TP3 at relative uncertainty magnitudes of 0.01, 0.1 and 0.2

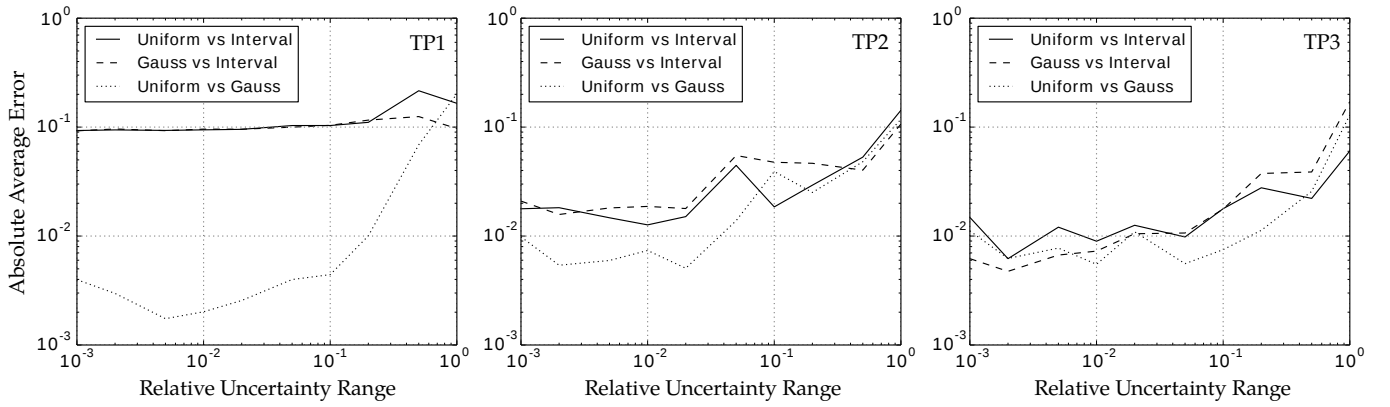


Figure 12: Average absolute errors between the heat-maps at different values of Δ_{rel} for the three test functions

space is multi-modal with several peaks and/or valleys then the overall landscape of Y dominates so that the “signal to noise ratio” is larger and the heat-maps become more similar.

For all three problems, as Δ_{rel} is increased, the heat maps become less similar. This is mainly seen as further distortion of the heat-map peaks compared to one another (while they remain roughly in the same location of design space), indicating an inverse relationship between the non-linearity of the local uncertainty landscape of Y and the similarity of UQ methods to a robust optimization.

Observations about the multimodality in a robust optimization are also made: TP3 is the most multimodal to a deterministic optimizer, containing two distinct optima and several valleys, whereas TP2 becomes the most multimodal to a robust optimizer. TP1 also changes from being distinctly unimodal to having a large area of design space of interest to the optimizer. This indicates how the design space of a unimodal problem can become more multi-modal and complex when robustness is introduced, which reflects the fact that performance and robustness often represent conflicting objectives so a larger amount of design space becomes of interest to an optimizer.

3.4.2 Average Errors

To quantify how similar/different the heat-maps are (measuring the signal to noise ratio), the average absolute difference between the probability values of two heat-maps over the design space is evaluated numerically (using a grid of 50 by 50 points). However, the value is only logged if both heat-map probability values are greater than 0.01, so that accumulation errors over large areas on the heat-maps that are of little interest to the optimizer are avoided. This average error is plotted for different values of Δ_{rel} on Figure 12; each point is the result of 50 NSGA-II robust optimization runs. Even though the

graphs are not fully smooth, and some noise exists due to the stochastic nature of how the heat-maps are formed, overall trends can still be observed.

We can identify the influence of both mechanisms discussed in section 3.1 on these plots. The first effect gives rise to the overall shape of the curves seen on all three plots where there is a positive relationship between Δ_{rel} and the difference between the heat-maps, whereas the second effect causes the three curves on each plot to become less spread out as the multi-modality of the function increases from TP1 to TP3.

For all three test problems, considering the probabilistic uncertainties, the uniform vs Gauss error follows a similar shape and similar values (beginning at $< 10^{-2}$, and ending at $\simeq 10^{-1}$), further demonstrating that increasing the non-linearity of the objective function with respect to the uncertainties means that the UQ method affects a robust optimization more.

For TP2 and especially TP3, considering the interval vs probabilistic lines, the effect of figure 7 is effectively drowned out by the multi-modality of the function so that all three lines follow the same pattern - the same as the gauss vs. uniform line on the TP1 plot.

This algebraic investigation demonstrates that the amount that the uncertainty representation affects a robust optimization depends on several factors: the number of uncertainties, the non-linearity of the objective function with respect to the uncertainties, whether the orientation of Y as a function of the uncertainties varies in design space, and the multi-modality of the problem. In this section we have identified the influence of each of these on the robust optimization of three algebraic test problems.

3.5 Significance of Algebraic Investigations

This section has given insight into the mechanisms by which differing uncertainty representations give rise to different results in a robust optimization. We offer discussion in terms of an effective signal to noise ratio, where the signal is the design landscape under the true representation of uncertainty, and the noise is the distortion to this landscape due to using a different representation.

Ideally, there would be some sort of test a designer could perform before doing an optimization to quantify what this signal to noise ratio would be for a particular problem, but due to each engineering design problem being non-linear in its own unique way, we envisage attempting to design such a test to not be a fruitful endeavor. Instead, we offer this qualitative insight so that if a designer has a conceptual understanding of the physical drivers present in a problem, they can make an informed decision as to how much effort should be spent on ensuring they are using the correct representation of the uncertainties.

In this paper we are interested in airfoil shape optimization, and so we apply this process to two design cases. Firstly an exploratory problem that is known to give a strong trade-off between performance and robustness: the inviscid lift to drag ratio maximization of a NACA0012 airfoil in the transonic regime. Secondly a practical airfoil design problem: a lift and geometrically constrained drag minimization of an RAE2822 airfoil in the transonic regime.

4 Robust Airfoil Lift to Drag Maximization

The first test problem considered in this paper concerns the unconstrained maximization of the lift to drag ratio of an airfoil in inviscid flow conditions. This problem is not intended to represent practical aerofoil design, since inviscid flow does not capture the full physical behavior and the conditions are not necessarily representative of a typical aircraft operating point, rather this problem is chosen to explore the ideas developed in section 3 because similar problems considered in the literature have been shown to give a strong trade-off between performance and robustness [18,34]. This allows us to examine the similarity of a whole Pareto front instead of a single optimum design, and allows us to apply the insights developed in the algebraic investigations.

4.1 Computational Approach

The drag at a given Mach number is determined using the SU2 open source CFD solver to solve the compressible Euler equations; SU2 has been well documented and validated on a number of test cases [35]. A baseline mesh (provided by SU2 for a NACA0012 transonic flow inviscid test case) consisting of 10,216 triangular cells made from 5,233 points is deformed to bound the new surface defined by the Hicks-Henne bump amplitudes using the mesh deformation code available within SU2. A zoomed in snapshot of the baseline mesh around the airfoil is shown in figure 13, and it extends to a circular farfield boundary of radius 20 chord lengths. The solver is run until the density residual has reached 10^{-6} , which is enough to give lift and drag coefficients to 3 significant figures.

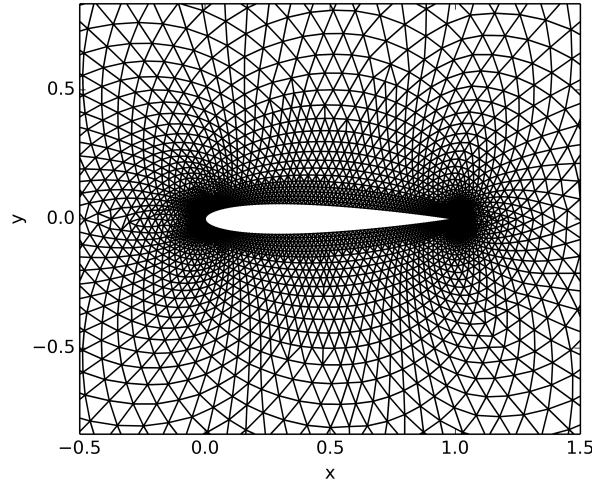


Figure 13: Close-up of the baseline mesh for the undeformed NACA0012 airfoil.

To validate the adequacy of this mesh and the SU2 solver, it is compared to results given in [36], where the flow field for transonic flow over the NACA0012 airfoil obtained using the well known FLO82 solver and a very fine mesh resolution is presented. Figure 14 gives the surface pressure coefficient plots from [36] along with those obtained using the SU2 setup for this paper; the flow conditions are Mach 0.8 and an angle of attack of 1.25° .

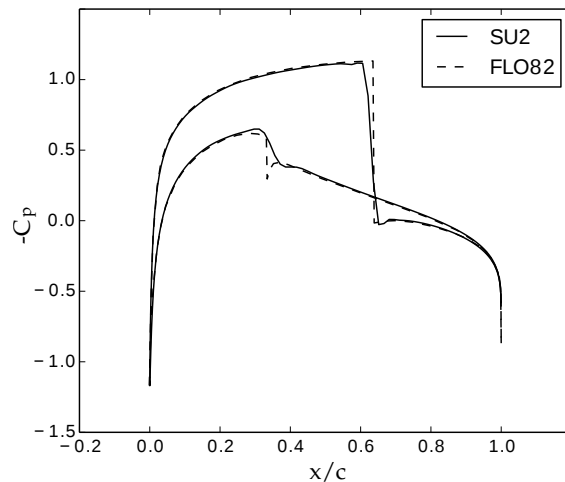


Figure 14: Comparison of the SU2 solver on the baseline mesh at $M=0.8$ and $\alpha=1.25$ with the FLO82 solver on an extremely fine 4096x4096 mesh (taken from [36]).

It is observed that away from the shocks the pressure distribution is well captured using the SU2 solver on the baseline mesh and that the locations of the shocks match the validation case. However, the shocks themselves are not as accurately captured; they are smeared over a larger distance along the surface. However, the overall pressure distribution is captured well and so this solver is sufficient for the purposes of this study: we do not require highly accurate numerical results, rather we require the solver to capture the key flow features that give rise to the behavior of an airfoil under the uncertainties.

4.2 Optimization Setup

The shape parameterization is achieved using Hicks-Henne bump functions at different chord locations on both surfaces of a NACA-0012 baseline airfoil, and the amplitudes of these bumps constitute the design space of the optimization. The locations of the Hicks-Henne bumps and their design ranges are given in table 1.

Table 1: Surface, location, and max/min amplitudes of Hicks-Henne bump functions for the airfoil shape parametrization (both as a fraction of chord length).

Surface	Location	Design Range
U	0.05	$\pm 1 \times 10^{-3}$
U	0.15	$\pm 6 \times 10^{-3}$
U	0.30	$\pm 9 \times 10^{-3}$
U	0.45	$\pm 9 \times 10^{-3}$
U	0.60	$\pm 6 \times 10^{-3}$
U	0.80	$\pm 2 \times 10^{-3}$
L	0.10	$\pm 1 \times 10^{-3}$
L	0.30	$\pm 7 \times 10^{-3}$
L	0.55	$\pm 7 \times 10^{-3}$
L	0.80	$\pm 2 \times 10^{-3}$

The uncertainties for this problem were set up to be similar to previous studies in the literature that consider multiple uncertainties over a smaller range than the drag minimization problem that will be considered in Section 5 (e.g. [18, 23, 34, 37, 38]). Here we consider uncertainties in Mach Number, Angle of Attack, and a shape design variable. Realistically, all the shape design variables will have similar uncertainties due to manufacturing tolerances but, especially for this problem, only a few will significantly impact the performance: those on the upper surface that influence the shock location. Therefore to keep the dimensionality of the problem reasonable, but still capturing the key behavior, only one shape uncertainty is taken into account, which is on the amplitude of the Hicks-Henne bump function at 45% chord on the upper surface. Similarly to Section 3, we only consider three uncertainty representations for clarity: uniform, interval and Gaussian.

Table 2: Uncertain variables and their distributions for the airfoil robust design problem.

Uncertain Variable	Interval / Uniform	Normal
Mach No.	[0.66, 0.70]	$N(0.68, \frac{0.02^2}{\sqrt{3}})$
AoA	[4.9, 5.1]	$N(5, \frac{0.1^2}{\sqrt{3}})$
HH Amp.	[-0.001, 0.001]	$N(0, \frac{0.001^2}{\sqrt{3}})$

The optimization is setup as a minimization problem that minimizes both f_p and f_r for $-L/D$:

$$\begin{aligned} & \underset{\mathbf{x}}{\text{minimize}} && [f_p(-L/D(\mathbf{x}, \mathbf{u})), f_r(-L/D(\mathbf{x}, \mathbf{u}))] \\ & \text{subject to} && x_i^l \leq x_i \leq x_i^u \quad i = 1, \dots, n_x \end{aligned} \quad (6)$$

where \mathbf{u} consists of the uncertainties given in Table 2, and the NSGA-II optimizer is run for 30 generations of populations of 60 candidates.

We solve this multi-objective optimization problem using the same NSGA-II algorithm that was used in Section 3, and it is run for 30 generations using populations of 60 candidates. To aid the optimizer, the Hicks-Henne bump amplitude design variables are normalized with respect to their bounds so that the optimization algorithm itself deals with 10 design variables that all have the same bounds (0.0 to 10.0). This allows the combination and mutation operators to work over an appropriately scaled design space. Additionally, we first run a deterministic optimization (using NSGA-II with a single objective of $L/D(\mathbf{x}, 0.68)$).

4.3 Polynomial Chaos Convergence

To establish the order of the NIPC expansion required to accurately capture the behavior of L/D due to the uncertainties, a convergence study is shown here. This is done for a design taken from the Pareto front found in a preliminary study, since this exhibits complex behavior likely to be encountered for solutions on the final Pareto front, more so than the baseline NACA0012 airfoil.

Figure 15 gives the PDF of L/D (obtained using a kernel density estimate from 30,000 samples of the NIPC response surface) as the order is increased, and Figure 16 gives the relative error of the mean and standard deviation estimates compared to the 6th order expansion's estimates. The number of CFD calls required to train each expansion using tensor product quadrature is $(p+1)^3$ where p is the order, and so increasing the order comes at a large computational cost.

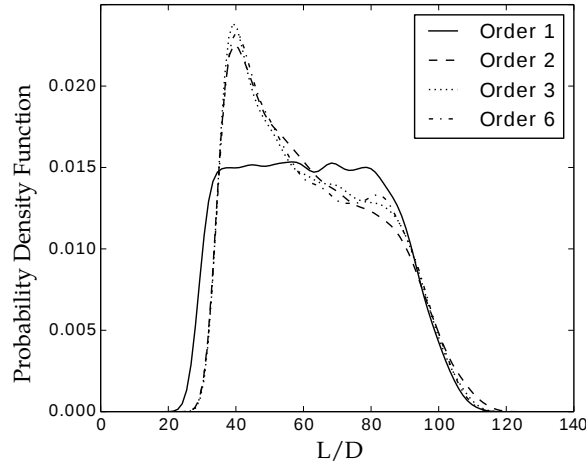


Figure 15: Convergence of the NIPC expansion PDFs under 3 uniformly distributed uncertainties.

From this convergence study, it appears that at least an order 3 expansion would be sufficient to capture the response accuracy (mean and variance within less than 0.01% of the 6th order values and a visibly matching PDF), requiring 64 CFD calls for each design candidate to propagate the uncertainty. Visible matching of the PDFs indicates convergence of the underlying 3-dimensional response surface to the CFD response over the uncertainty range, which is what matters for capturing the output interval and the non-linearity of the output with respect to the uncertainties; this is also deemed sufficient under an order 3 expansion.

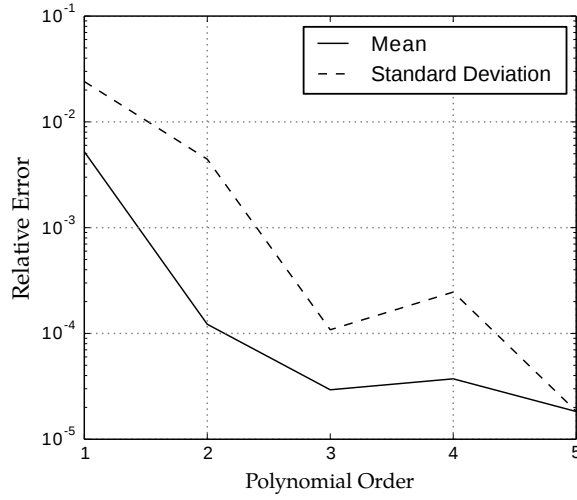


Figure 16: Convergence of the mean and standard deviation estimates from the PC expansion to those obtained with a 6th order expansion under 3 uniformly distributed uncertainties

The computational cost of each overall optimization is reduced using a variable order expansion method; this involves using a 1st order expansion for the first part of the optimization in order to quickly find regions in design space where non-dominated designs are likely to be found, and then switching to a 3rd order expansion for the last part of the optimization in order to accurately capture the desired Pareto front. For these optimizations, the order was increased after 15 generations.

4.4 Insight from the Algebraic Investigations

Using the results of Section 3, we can make predictions about the signal to noise ratio for this problem. The behavior of lift and drag as functions of Mach number, angle of attack and the shape parameter are expected, for feasible designs, to not be significantly non-linear over the range of the uncertainties, which is most comparable to low Δ_{rel} values on the test problems.

Furthermore, the uncertainties in this airfoil design problem include two design parameters and only one design variable, so we expect the effect from Figure 7 to not be significantly different between designs. The multi-modality of aerodynamic shape optimization is discussed in [39], where it is illustrated that typical 2-D airfoil optimization problems are unimodal to deterministic optimizations, so we do not expect the signal to noise ratio to be improved by multi-modality of the problem. However, from consideration of the other mechanisms we can be reasonably confident that the signal to noise ratio will be high for this problem and so we expect designs on the Pareto fronts resulting from optimizations under different uncertainty representations to be similar.

4.5 Results

Since we are actually interested in the designs on each Pareto front (the corresponding Pareto set) and not the values of f_p and f_r on the fronts themselves, we evaluate the designs from the Pareto set resulting from each optimization under uniformly distributed uncertainty and plot them all on the same $\mu_{L/D}$ vs $\sigma_{L/D}$ graph, given in figure 17.

Also, in order to further examine the underlying designs, we look in more detail at designs from each Pareto set which, when analysed under uniform uncertainties, are very close in objective space at three locations along the Pareto front (labeled on Figure 17 as selected designs). The relevant f_p and f_r using the different UQ methods for the three designs taken from the uniform front (alongside the deterministic optimum) are given in table 3, the PDFs of these are plotted in figure 18, and the surface pressure distributions of the selected designs from all three fronts are plotted on figure 20.

From Figure 18 it can be observed that all of the PDFs from the designs on the uniform Pareto front show non-linear behavior: they are skewed and some have two identifiable peaks. The PDF of the deterministic optimum design under Gaussian uncertainty is also given for comparison where it is less skewed than the uniform PDF with a more central peak,

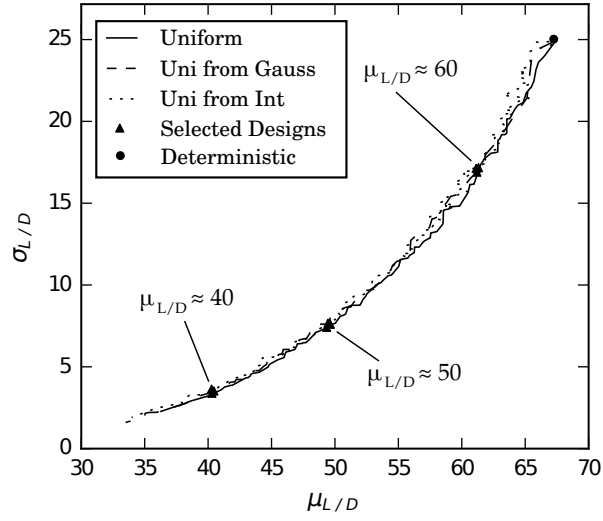


Figure 17: The three final robust Pareto optimal sets of designs under uniformly distributed uncertainty (plotted as continuous lines).

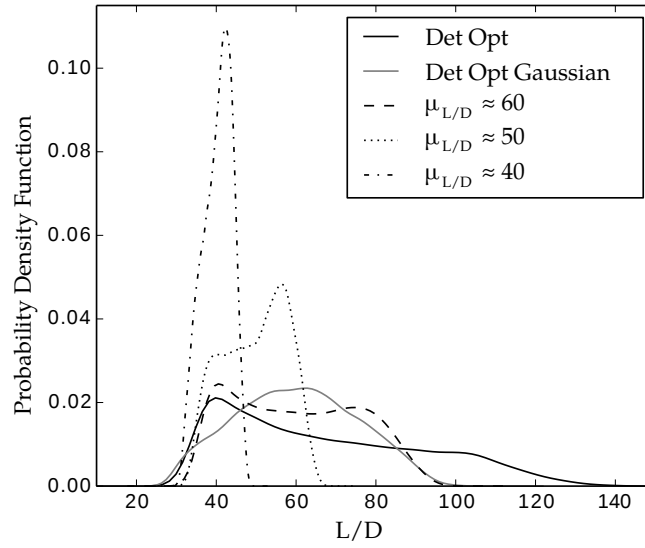


Figure 18: PDFs of the selected designs from the uniform Pareto front under uniform uncertainties along with that of the deterministic optimum under both uniform and Gaussian uncertainties.

Table 3: f_p and f_r of the selected designs from the uniform Pareto front when analyzed using the different UQ methods.

Selected Design	Det Opt	$\mu \simeq 60$	$\mu \simeq 50$	$\mu \simeq 40$
$\mu_{uniform}$	67.3	61.2	49.5	40.9
$\mu_{gaussian}$	66.6	61.0	49.6	41.0
$midpoint_{interval}$	88.2	69.0	48.7	39.2
$\sigma_{uniform}$	24.8	17.4	7.69	3.68
$\sigma_{gaussian}$	23.6	16.5	7.59	3.80
$range_{interval}$	112.0	72.6	32.8	31.9

and this propagated difference in structure of the uncertainty is what gives the different μ and σ values under the different probabilistic uncertainties observed in table 3. Note that under interval uncertainties, none of this structure is propagated.

Despite the differences in the output uncertainty information propagated in each optimization, it is clear from Figure 17 that all three Pareto fronts collapse onto similar curves when analyzed under the same type of uncertainty, suggesting that similar designs have been found by all three optimizations (agreeing with our prediction in section 4.4).

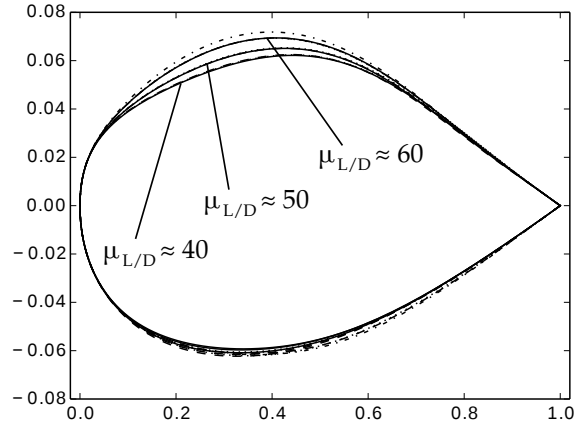


Figure 19: Corresponding airfoil shapes for the selected designs on Figure 17.

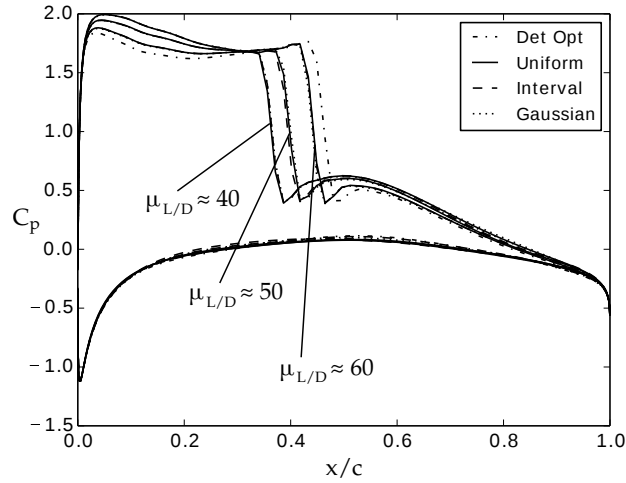


Figure 20: Surface pressure distributions for the selected airfoils from the Pareto fronts that have similar μ and σ under uniform uncertainties: $\mu_{L/D} \simeq 40$, $\mu_{L/D} \simeq 50$, $\mu_{L/D} \simeq 60$.

The airfoil shapes and surface pressure distributions on figures 19 and 20 further demonstrate the similarity of the designs, in that their shapes are visibly similar and the same underlying physical mechanism driving the performance vs robustness trade-off is captured well by all three robust optimizations. In this case, the Pareto optimal designs have similar pressure distributions over the lower surface and the leading and trailing edge of the upper surface, however the location of the shock determines where along the robust Pareto front the design is. Higher mean L/D airfoils have the shock further aft compared to more robust airfoils, and this is seen regardless of how the uncertainty is quantified.

5 Robust Airfoil Drag Minimization

The second design problem considered is a drag minimization subject to lift and geometry constraints and Mach number uncertainty; this reflects a practical airfoil design problem commonly considered in the literature [2, 3, 13, 16, 40, 41].

5.1 Computational Approach

The drag at a given Mach number is determined using the SU2 open source CFD solver to solve the compressible RANS equations. The Reynolds number is set to 6.5×10^6 and the Spalart-Allmaras turbulence model is used. The design space is parameterized using Hicks-Henne bump functions: for each design a baseline mesh (provided by SU2 for a RAE2822 transonic RANS test case), consisting of an unstructured mesh made up of 13937 points, is deformed to bound the new surface defined by the Hicks-Henne bump amplitudes using the mesh deformation code available within SU2. A zoomed in snapshot of the baseline mesh is given in Figure 21, and it extends to a circular farfield boundary of radius 100 chord lengths. This mesh is one of the cases in [35] used to validate SU2, where it shows good agreement with experimental data at transonic conditions, so we do not repeat a comparison here. Again, the solver is run until the density residual is below 10^{-6} , which is enough to give lift and drag coefficients to 3 significant figures.

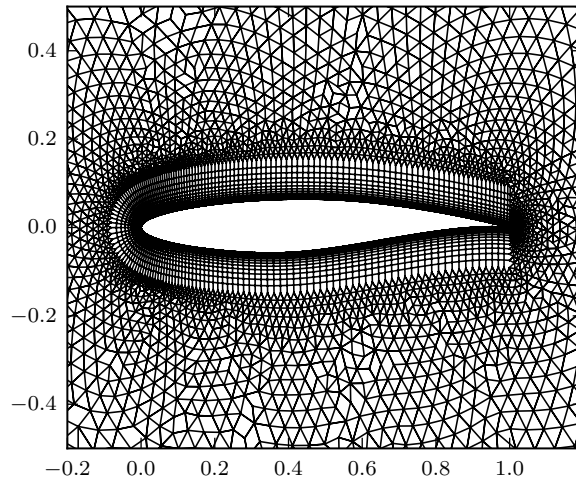


Figure 21: Baseline mesh for the RAE2822 airfoil

5.2 Optimization Setup

For this problem we consider a lift constraint where $C_L = 0.4$ and a geometry constraint where a torsion box of dimension 0.5×0.75 chord lengths that just fits inside the initial RAE2822 geometry must also fit inside any new design, representing structural requirements. The design space is parameterized using the 14 Hicks-Henne bump functions given in Table 4 along with their bounds (which define the limits of design space).

We consider uncertainty in Mach number, which embodies uncertainty over a range of operating conditions, and all four uncertainty representations: Mach number is uncertain over the interval $[0.7, 0.8]$ for uniform, beta and interval uncertainty representations and distributed according to $N(0.75, 0.1/\sqrt{3})$ for the Gaussian representation (as described in Section 2.1).

At each Mach number, the angle of attack is adjusted so that $C_L = 0.4$ (it is iterated until the calculated value is within ± 0.0005 of 0.4), and since the constraints are not affected by the uncertainty, we retain the robust optimization formulation proposed in Section 1 where it is the impact of uncertainties on the objective function that is of interest. Therefore we are

Table 4: Surface, location, upper and lower bounds of Hicks-Henne bump functions for the airfoil shape parametrization (all as a fraction of chord length)

Surface	Location	Upper Bound	Lower Bound
U	0.05	10×10^{-3}	-10×10^{-3}
U	0.20	10×10^{-3}	-15×10^{-3}
U	0.40	10×10^{-3}	-20×10^{-3}
U	0.60	10×10^{-3}	-20×10^{-3}
U	0.75	10×10^{-3}	-5×10^{-3}
U	0.86	10×10^{-3}	-5×10^{-3}
U	0.93	10×10^{-3}	0×10^{-3}
L	0.05	10×10^{-3}	-10×10^{-3}
L	0.20	10×10^{-3}	-20×10^{-3}
L	0.40	10×10^{-3}	-25×10^{-3}
L	0.60	10×10^{-3}	-10×10^{-3}
L	0.75	10×10^{-3}	-5×10^{-3}
L	0.86	10×10^{-3}	0×10^{-3}
L	0.93	10×10^{-3}	0×10^{-3}

solving the following optimization problem:

$$\begin{aligned}
& \underset{\mathbf{x}}{\text{minimize}} && [f_p(C_D(\mathbf{x}, M)), f_r(C_D(\mathbf{x}, M))] \\
& \text{subject to} && x_i^l \leq x_i \leq x_i^u \quad i = 1, \dots, n_x \\
& && C_L(\mathbf{x}, M) = 0.4 \\
& && z(\mathbf{x}) \leq 0
\end{aligned} \tag{7}$$

where $z(\mathbf{x})$ is the protrusion of the torsion box outside the surface geometry for a given design.

We solve this multi-objective optimization problem using the NSGA-II algorithm, which is run for 50 generations using populations of 50 candidates. We first run a deterministic optimization (using NSGA-II with a single objective of $C_D(\mathbf{x}, 0.75)$ for 100 generations).

5.3 Polynomial Chaos Convergence

To establish the order of the NIPC expansion required to accurately capture the behavior of drag due to the uncertainties, a convergence study is shown here: this is done for the baseline RAE2822 airfoil. Figure 22 gives the PDF of C_D (obtained using a kernel density estimate from 30,000 samples of the NIPC response surface) as the order is increased, as well as the relative error of the mean and standard deviation estimates compared to a 6th order expansion's estimates. The number of CFD solves required to train each expansion is $(p + 1)$ where p is the order.

From these results, a 4th order NIPC expansion (requiring CFD evaluations at 5 Mach numbers) is deemed to be sufficiently accurate, and so is used throughout the optimizations.

5.4 Insight from the Algebraic Test Problems

For this test problem, we are considering a fairly large uncertain Mach number range which includes the transonic drag rise. This is illustrated in Figure 24 where the drag polar over Mach number for the RAE2822 baseline design is plotted.

There is a significant drop off in performance for the baseline design over the upper half of the uncertainty range, and so we expect a robust optimization to give significant benefit, not only over this baseline case but also over the deterministic optimum which only considers $M = 0.75$. Additionally, since this drag rise is a significant non-linearity, giving a more skewed

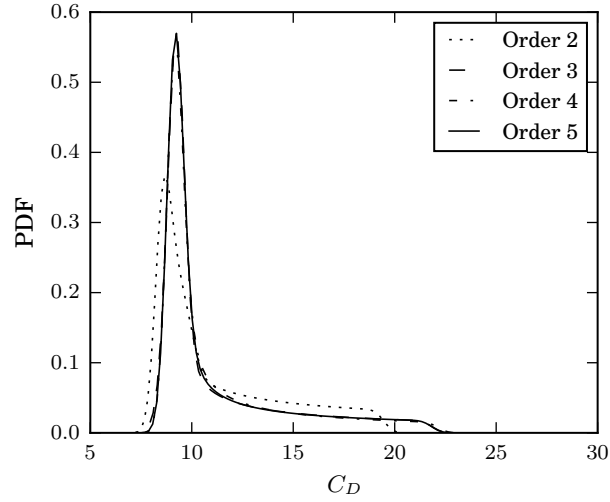


Figure 22: Convergence of PDF from the NIPC expansion when Mach number is uniformly distributed over $[0.7, 0.8]$ for the baseline design

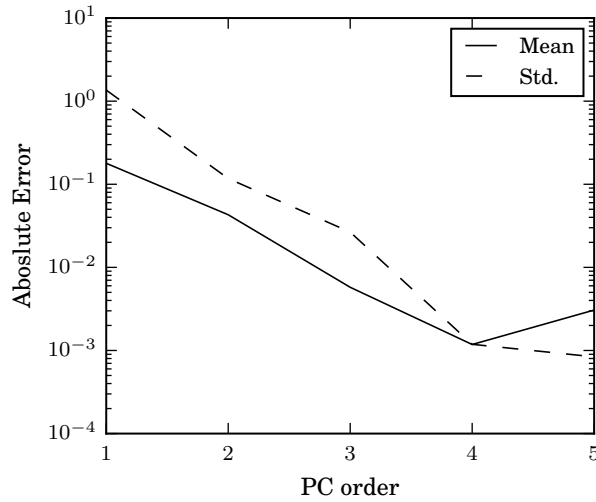


Figure 23: Convergence of moments from the NIPC expansion when Mach number is uniformly distributed over $[0.7, 0.8]$ for the baseline design.

PDF of the objective than the previous test problem (compare figure 22 with figure 15), we do expect the representation of uncertainty to have an impact on the results of the robust optimizations and so do not expect the same optimum under each representation of the uncertainty. This would agree with a previous brief investigation on the impact of using different PDFs for Mach number on robust airfoil optimization [15], nevertheless we do expect that the same physical drivers giving rise to the robustness of the optimum airfoils to be captured in all four cases.. Additionally, since only one uncertainty is present the effect from Figure 7 will not play a role. Therefore, while we do not expect the same optimum design in each case, we do expect the signal to noise ratio discussed in Section 3.4 to be high.

5.5 Results

On Figure 25, we plot all points from the optimization under each type of uncertainty in the corresponding objective space in grey. The first observation is that there is a weak trade-off between f_p and f_r for this design problem. The trade-off does vary between the uncertainty representations, with the largest trade-off being found under Gaussian uncertainty, but the

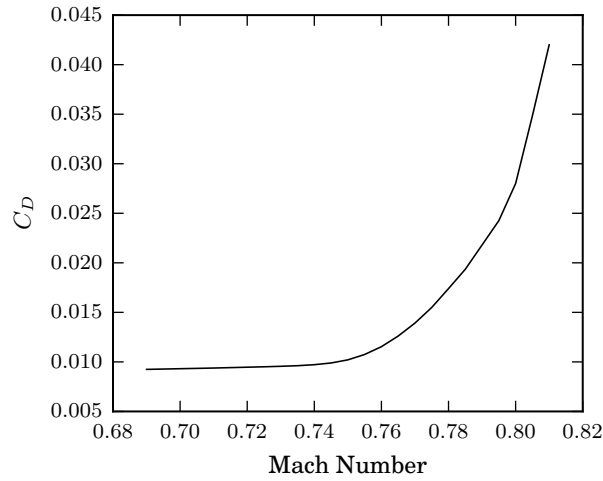


Figure 24: Drag polar for RAE2822 airfoil for $C_L = 0.4$

Pareto front is still small and only a few designs are of interest. This result is interesting in itself, since it implies that for drag-minimization based airfoil design, only considering expected performance (or interval midpoint) is sufficient to also obtain a robust design. This is likely because when considering only the drag at a given lift coefficient over Mach number, delaying the drag rise is the main physical driver for improving the expected value since there is such a sharp drop off in performance after its onset, but this is also the main driver for reducing the variance/interval range.

Therefore for comparison the design that is closest to the origin for each uncertainty case is taken as the optimum design for that case. Then to compare the similarity of these designs, they are analyzed under all four uncertainty representations and the resulting f_p and f_r values are plotted in objective space on the corresponding plots. The baseline RAE2822 design is also plotted on these points as the grey diamond. Additionally on Figure 26 we give the convergence of these NSGA-II optimizations, in terms of distance of the closest point to the origin.

We compare the airfoil shapes corresponding to the optimum design in each case on Figure 27, and to further investigate the similarity of the designs we plot the corresponding drag polars over Mach number on Figure 28.

From these results, we can see that the airfoil shapes give rise to noticeably different drag polars. The beta optimum has the worst performance at higher Mach numbers since the PDF places the least emphasis on these conditions out of the uncertainty representations, the interval has the best, and the uniform and gauss optimum lie between these two (similar results are obtained in [15]). The deterministic optimum has the best performance at the nominal Mach number of 0.75 but sees a severe drop in performance at higher Mach numbers. It is also noticeable that the drag polars of these optimum designs are similar to those of airfoils optimized using the multi-point approach in the literature. For example, in [14], a multi-point optimization of the RAE2822 airfoil subject to thickness constraints and $C_L = 0.733$ (at Mach numbers 0.68, 0.71, 0.74, and 0.76, with corresponding weights 1, 1, 2, and 3) is performed. The absolute values of the drag polar for the optimum design are different, but its shape compared to the RAE2822 is similar to the robust optimum designs obtained in this study. As discussed in section 2.2.2, an NIPC estimate of the expected performance is essentially a multi-point method with the points and weights chosen to optimally integrate over the input PDF. Since for this problem there is limited trade-off between mean performance and robustness, the optimal robust design chosen in each case is close to the minimum mean design, so we would also expect a multi-point approach to produce a similar optimum design to those obtained here.

However, the most significant result for this study is that when the four optimum designs are analyzed under the same uncertainty they are close together in objective function space, and importantly they are closer together than the distance to the deterministic optimum from any of the designs. In essence, the ratio of the distance of the group from the deterministic optimum to the maximum distance between designs in the group quantifies the signal to noise ratio from a designer's point of view; this is annotated on Figure 25b. Further, all four cases Pareto dominate the deterministic optimum, and so we

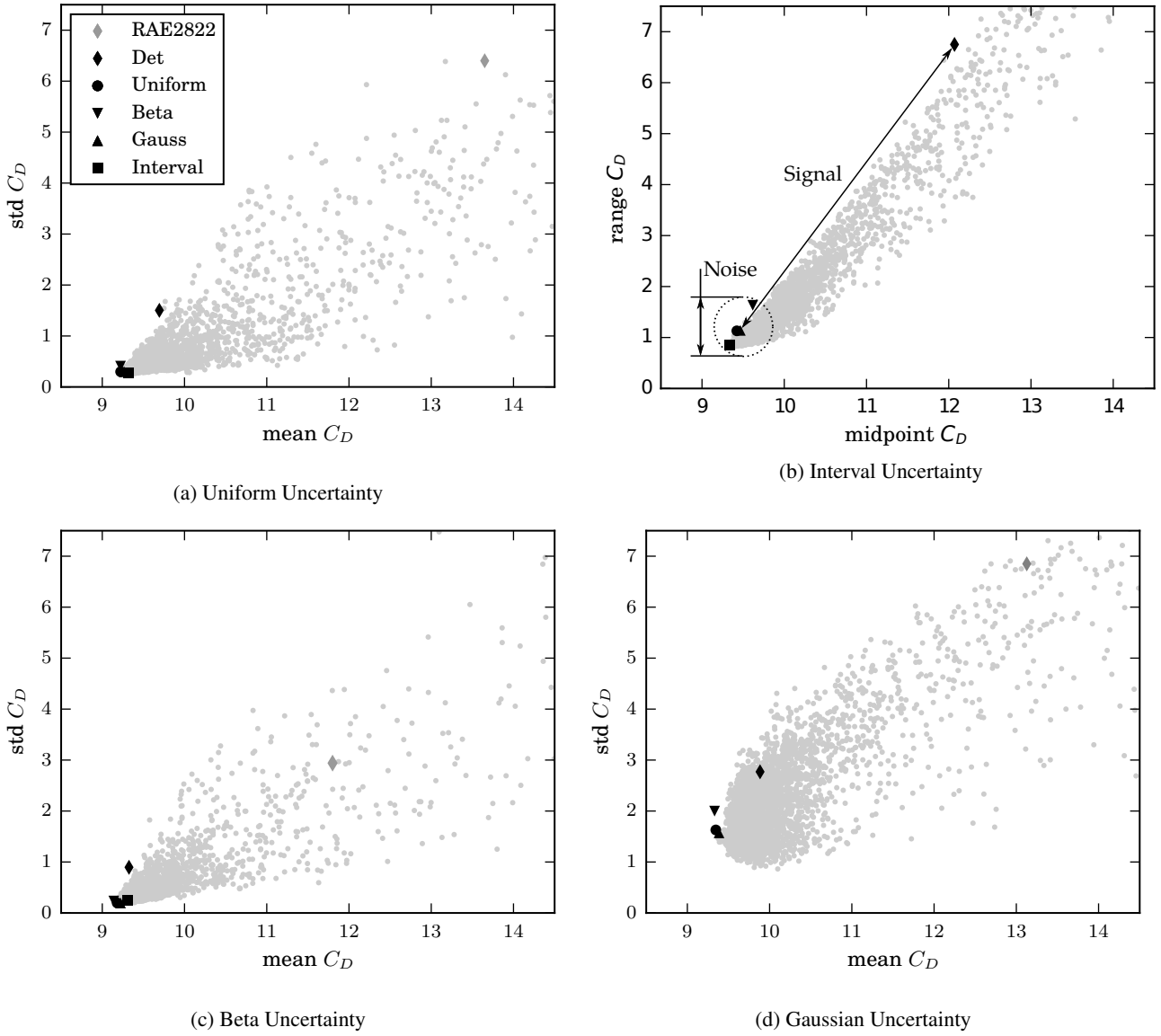


Figure 25: Results of the robust optimization when the uncertainties are represented mathematically in four different ways (grey), along with the optimum design from each optimization analyzed with the corresponding representation (black).

can conclude that for this robust airfoil design case, the benefit of performing a robust optimization over a deterministic optimization is similar regardless of how the input uncertainties are quantified mathematically.

6 Conclusions

In this paper we have presented an investigation aimed at shedding some light on the question "to what extent does the mathematical representation of uncertainty affect the results of a robust optimization?", specifically concerning robust airfoil design. Clearly, this question cannot be answered in a general sense, since different engineering design problems exhibit different non-linear characteristics. However, in this paper we offer insight, in terms of a signal to noise ratio, into the mechanisms by which different representations of uncertainty can affect the results of robust optimizations by performing a large number of optimizations on algebraic test problems. Through this we are able to obtain useful conclusions for robust airfoil optimization by applying this insight to an exploratory lift to drag ratio maximization airfoil design case and a practical lift and shape constrained drag minimization airfoil design case.

Our main conclusion is that, for typical magnitudes of uncertainty, the benefit of performing a robust optimization for

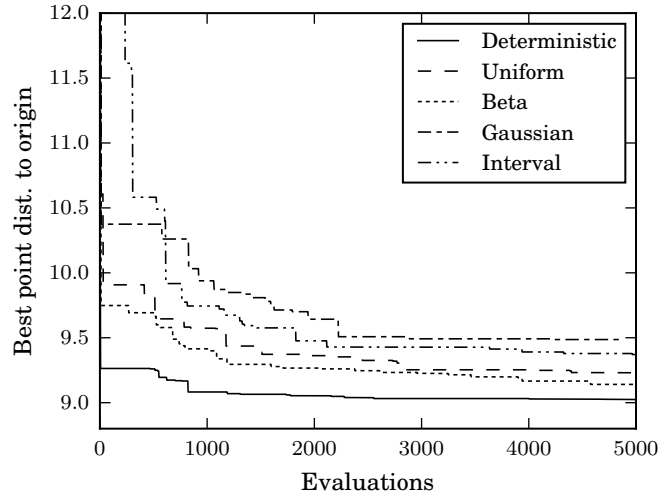


Figure 26: Convergence of NSGA-II for the five optimization cases.

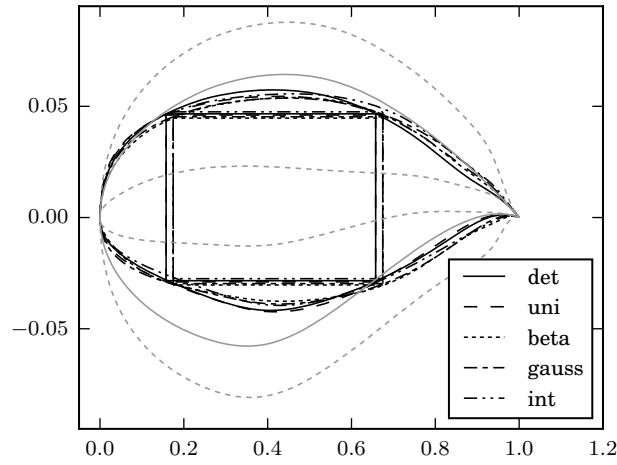


Figure 27: Comparison of optimum airfoil designs, as well as the bounds on design space (dashed grey) and initial RAE2822 design (solid grey).

airfoil design over a deterministic optimization (the signal) is large compared to the differences between optimum designs arising due to mis-representing the uncertainty (the noise). For the unconstrained lift to drag ratio maximization in Section 4, this manifested as similar Pareto sets being obtained under different uncertainty representations in contrast to the single design obtained from the deterministic optimization. For the constrained drag minimization problem in Section 5, this manifested as the grouping of the optimum designs under different uncertainty representations in f_p/f_r space being small compared to the group's distance from the deterministic optimum, which was also Pareto dominated by the group.

Since the noise introduced by uncertainty representation is not zero, this work is perhaps most relevant to preliminary stages of design, where the result of a robust optimization will be progressed on to further design stages for refinement and so an exact design is not required. One objective in providing this investigation is in order to potentially save designers' time (which is especially important at the preliminary stages of design): since accurately representing input uncertainties can be a considerable undertaking. The significance of preliminary design in determining final achieved system performance has been observed in other application areas (e.g. turbomachinery [42]). The results of this paper suggest that for airfoil design a significant benefit may be gained from robust optimization in the preliminary design phase under different mathematical representations of the uncertainty, both over the initial design and over not considering uncertainties at all.

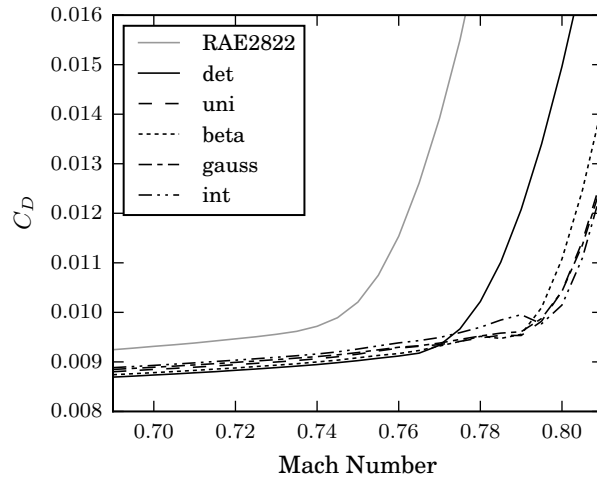


Figure 28: Comparison of drag polars for the optimum airfoil designs. $C_L = 0.4$

A limitation of this study is that it considers comparable symmetric uncertainty representations - over the same interval in the case of uniform vs. beta vs. interval and a Gaussian distribution with the same standard deviation as the uniform one - all centered around the same central value. Therefore we acknowledge (as shown in [15] where skewed distributions are considered), moving the nominal value as well as the range of the uncertainties will have an impact on the result of the optimization, and therefore future work should investigate in more detail the relative impact of these changes.

However the focus of the current work is on the mathematical representation, suggesting that certain quantities about the uncertainty, such as nominal value and range, have already been prescribed, and a designer has to decide whether further investigation into the “true” representation of uncertainty is warranted, essentially progressing the uncertainty from epistemic towards being purely aleatory. We have shown that for robust airfoil shape optimization this may not be necessary, especially at a preliminary design level where it is the key design features that need to be captured.

Acknowledgment

The authors would like to thank the UK Engineering and Physical Sciences Research Council for the funding supporting this research.

References

- [1] Keane, A. J. and Nair, P. B., *Computational Approaches for Aerospace Design: The Pursuit of Excellence*, Wiley, New York, 2005.
- [2] Drela, M., “Pros and Cons of Airfoil Optimization,” *Proceedings of Frontiers of Computational Fluid Dynamics*, D.A. Caughey, M.M. Hafez, Eds., World Scientific, ISBN 981-02-3707-3, 1998, pp. 1–19.
- [3] Huyse, L., Padula, S., Lewis, M., and Li, W., “Probabilistic Approach to Free-Form Airfoil Shape Optimization Under Uncertainty,” *AIAA Journal*, Vol. 40, No. 9, 2002, pp. 1764–1772.
- [4] Kennedy, M. C. and O’Hagan, A., “Bayesian Calibration of Computer Models,” *Journal of the Royal Statistical Society. Series B (Statistical Methodology)*, Vol. 63, No. 3, 2001, pp. 425–464.
- [5] Beyer, H. G. and Sendhoff, B., “Robust Optimization - A Comprehensive Survey,” *Computer Methods in Applied Mechanics and Engineering*, Vol. 196, No. 33-34, 2007, pp. 3190–3218.
- [6] Kiureghian, A. D. and Ditlevsen, O., “Aleatory or Epistemic? Does It Matter?” *Structural Safety*, Vol. 31, No. 2, 2009, pp. 105–112.
- [7] Helton, J. C., Johnson, J. D., and Oberkampf, W. L., “An Exploration of Alternative Approaches to the Representation of Uncertainty in Model Predictions,” *Reliability Engineering and System Safety*, Vol. 85, No. 1-3, 2004, pp. 39–71.
- [8] Hoffman, F. O. and Hammonds, J. S., “Propagation of Uncertainty in Risk Assessments: The Need to Distinguish

Between Uncertainty Due to Lack of Knowledge and Uncertainty Due to Variability,” *Risk Analysis*, Vol. 14, No. 5, 1994, pp. 707–712.

- [9] Hosder, S. and Bettis, B., “Uncertainty and Sensitivity Analysis for Reentry Flows with Inherent and Model-Form Uncertainties,” *Journal of Spacecraft and Rockets*, Vol. 49, No. 2, 2012, pp. 193–206.
- [10] Kleb, B. and Johnston, C. O., “Uncertainty Analysis of Air Radiation for Lunar Return Shock Layers,” *Journal of Spacecraft and Rockets*, Vol. 49, No. 3, 2008, pp. 425–435.
- [11] Zhang, Y. and Hosder, S., “Robust Design Optimization Under Mixed Uncertainties With Stochastic Expansions,” *Journal of Mechanical Design*, Vol. 135, 2013.
- [12] Eldred, M. S., Swiler, L. P., and Tang, G., “Mixed Aleatory-Epistemic Uncertainty Quantification With Stochastic Expansions and Optimization-Based Interval Estimation,” *Reliability Engineering and System Safety*, Vol. 96, No. 9, 2011, pp. 1092–1113.
- [13] Li, W., Huyse, L., and Padula, S., “Robust Airfoil Optimization to Achieve Drag Reduction Over a Range of Mach Numbers,” *Structural and Multidisciplinary Optimization*, Vol. 24, No. 1, 2002, pp. 38–50.
- [14] Nemec, M., Zingg, D. W., and Pulliam, T. H., “Multipoint and Multi-Objective Aerodynamic Shape Optimization,” *AIAA Journal*, Vol. 42, No. 6, jun 2004, pp. 1057–1065.
- [15] Lurati, L., “Robust Airfoil Design Under Uncertain Operation Conditions Using Stochastic Collocation,” *46th AIAA Aerospace Sciences Meeting and Exhibit*, , No. M, 2008, pp. 1–10.
- [16] Croicu, A.-M., Hussaini, M. Y., Jameson, A., and Klopfer, G., “Robust Airfoil Optimization Using Maximum Expected Value and Expected Maximum Value Approaches,” *AIAA Journal*, Vol. 50, No. 9, 2012, pp. 1905–1919.
- [17] Buckley, H. P. and Zingg, D. W., “Approach to Aerodynamic Design Through Numerical Optimization,” *AIAA Journal*, Vol. 51, No. 8, 2013, pp. 1972–1981.
- [18] Dodson, M. and Parks, G. T., “Robust Aerodynamic Design Optimization Using Polynomial Chaos,” *Journal of Aircraft*, Vol. 46, No. 2, 2009, pp. 635–646.
- [19] Jin, Y. and Sendhoff, B., “Trade-Off Between Performance and Robustness : An Evolutionary Multiobjective Approach,” *Evolutionary Multi-Criterion Optimization*, 2003, pp. 237–251.
- [20] Keane, A. J., “Comparison of Several Optimization Strategies for Robust Turbine Blade Design,” *Journal of Propulsion and Power*, Vol. 25, No. 5, 2009, pp. 1092–1099.
- [21] Schuëller, G. I. and Jensen, H. A., “Computational Methods in Optimization Considering Uncertainties - An Overview,” *Computer Methods in Applied Mechanics and Engineering*, Vol. 198, No. 1, 2008, pp. 2–13.
- [22] Ferson, S., Joslyn, C. A., Helton, J. C., Oberkampf, W. L., and Sentz, K., “Summary From the Epistemic Uncertainty Workshop: Consensus Amid Diversity,” *Reliability Engineering and System Safety*, Vol. 85, No. 1-3, 2004, pp. 355–369.
- [23] Padulo, M., Campobasso, M. S., and Guenov, M. D., “Novel Uncertainty Propagation Method for Robust Aerodynamic Design,” *AIAA Journal*, Vol. 49, No. 3, 2011, pp. 530–543.
- [24] Ghisu, T., Parks, G. T., Jarrett, J. P., and Clarkson, P. J., “Adaptive Polynomial Chaos for Gas Turbine Compression Systems Performance Analysis,” *AIAA Journal*, Vol. 48, No. 6, 2010, pp. 1156–1170.
- [25] Xiu, D. and Karniadakis, G. E., “Modeling Uncertainty in Flow Simulations via Generalized Polynomial Chaos,” *Journal of Computational Physics*, Vol. 187, No. 1, 2003, pp. 137–167.
- [26] Nam, H. K., Wang, H., and Queipo, N. V., “Efficient Shape Optimization Under Uncertainty Using Polynomial Chaos Expansions and Local Sensitivities,” *AIAA Journal*, Vol. 44, No. 5, 2006.
- [27] Hosder, S., Walters, R. W., and Balch, M., “Point-Collocation Nonintrusive Polynomial Chaos Method for Stochastic Computational Fluid Dynamics,” *AIAA Journal*, Vol. 48, No. 12, 2010, pp. 2721–2730.
- [28] Le Matre, O. P., Knio, O. M., Najm, H. N., and Ghanem, R. G., “A Stochastic Projection Method for Fluid Flow,” *Journal of Computational Physics*, Vol. 173, No. 2, nov 2001, pp. 481–511.
- [29] Xiu, D. and Karniadakis, G. E. M., “The Wiener-Askey Polynomial Chaos for Stochastic Differential Equations,” *SIAM Journal on Scientific Computing*, Vol. 24, No. 2, 2002, pp. 619–644.

- [30] Rumpfkeil, M. P., “Robust Design Under Mixed Aleatory / Epistemic Uncertainties Using Gradients and Surrogates,” *Journal of Uncertainty Analysis and Applications*, 2013.
- [31] Du, X. and Chen, W., “Methodology for Managing the Effect of Uncertainty in Simulation-Based Design,” *AIAA Journal*, Vol. 38, No. 8, 2000.
- [32] Mirjalili, S. and Lewis, A., “Obstacles and Difficulties for Robust Benchmark Problems: A Novel Penalty-Based Robust Optimisation Method,” *Information Sciences*, Vol. 328, 2016, pp. 485–509.
- [33] Deb, K., Pratap, A., Agarwal, S., and Meyarivan, T., “A Fast and Elitist Multiobjective Genetic Algorithm: NSGA-II,” *IEEE Transactions on Evolutionary Computation*, Vol. 6, No. 2, 2002, pp. 182–197.
- [34] Seshadri, P., Constantine, P., Iccarino, G., and Parks, G., “A Density-Matching Approach for Optimization Under Uncertainty,” *Computer Methods in Applied Mechanics and Engineering*, 2016.
- [35] Palacios, F., Economou, T. D., Aranake, A. C., Copeland, S. R., Lonkar, A. K., Lukaczyk, T. W., Manosalvas, D. E., Naik, K. R., Padron, A. S., Tracey, B., Variyar, A., and Alonso, J. J., “Stanford University Unstructured (SU2): Open-source Analysis and Design Technology for Turbulent Flows,” *AIAA Journal*, Vol. 51, No. January, 2014, pp. 1–19.
- [36] Vassberg, J. C. and Jameson, A., “In pursuit of grid convergence for two-dimensional Euler solutions,” *Journal of Aircraft*, Vol. 47, No. 4, 2010, pp. 1152–1166.
- [37] Shah, H., Hosder, S., Koziel, S., Tesfahunegn, Y., and Leifsson, L., “Multi-fidelity Robust Aerodynamic Design Optimization Under Mixed Uncertainty,” *Aerospace Science and Technology*, Vol. 45, 2015, pp. 17–29.
- [38] Schulz, V. and Schillings, C., “Problem Formulations and Treatment of Uncertainties in Aerodynamic Design,” *AIAA Journal*, Vol. 47, No. 3, 2009, pp. 646–654.
- [39] Chernukhin, O. and Zingg, D. W., “Multimodality and Global Optimization in Aerodynamic Design,” *AIAA Journal*, Vol. 51, No. 6, 2013, pp. 1342–1354.
- [40] Padula, S. L., Gumbert, C. R., and Li, W., “Aerospace Applications of Optimization Under Uncertainty,” *Optimization and Engineering*, Vol. 7, No. 3, 2006, pp. 317–328.
- [41] Lee, S. W. and Kwon, O. J., “Robust Airfoil Shape Optimization Using Design for Six Sigma,” *Journal of Aircraft*, Vol. 43, No. 3, 2006, pp. 4–7.
- [42] Jarrett, J. P. and Ghisu, T., “Balancing Configuration and Refinement in the Design of Two-Spool Multistage Compression Systems,” *Journal of Turbomachinery*, Vol. 137, No. 9, 2015.